

Graphical Abstract

**Dynamical pressure boundary condition for weakly-compressible
smoothed particle hydrodynamics**

Shuoguo Zhang, Yu Fan, Dong Wu, Chi Zhang, Xiangyu Hu

Highlights

Dynamical pressure boundary condition for weakly-compressible smoothed particle hydrodynamics

Shuoguo Zhang, Yu Fan, Dong Wu, Chi Zhang, Xiangyu Hu

- A dynamical pressure boundary condition for the WCSPH method to impose constant or time-dependent pressure.
- A much simpler bidirectional in-/outflow buffer for the SPH method.
- Preliminary hemodynamic simulations on carotid and aorta flows with the Windkessel model.

Dynamical pressure boundary condition for weakly-compressible smoothed particle hydrodynamics

Shuoguo Zhang^a, Yu Fan^a, Dong Wu^a, Chi Zhang^a, Xiangyu Hu^{a,*}

^a*School of Engineering and Design, Technical University of Munich, Garching, 85748, Germany*

Abstract

This paper introduces a novel dynamical pressure boundary condition for weakly-compressible smoothed particle hydrodynamics (WCSPH). Unlike previous methods that rely on indirect approaches or ghost particles, our method integrates the dynamical boundary pressure directly into the SPH approximation of the pressure gradient on near-boundary particles. Additionally, we develop a meshfree bidirectional in-/outflow buffer by periodically relabelling buffer particles at each time step, a concept that has not been explored before. This simple yet effective buffer facilitates the simulation of both uni- and bidirectional flows, especially those with mixed in-/outflow boundary conditions. We validate the accuracy and convergence of our method through benchmark cases with available analytical solutions. Furthermore, we demonstrate its versatility in hemodynamic simulations by investigating generic carotid and aorta flows with the Windkessel model, paving the way for studying the cardiovascular system within a unified mesh-free computational framework.

*Corresponding author

Email address: `xiangyu.hu@tum.de` (Xiangyu Hu)

Keywords: Pressure boundary condition, In-/outflow buffer, Open boundary, Weakly-compressible SPH, Windkessel model

1. Introduction

The hemodynamic flows, as typical incompressible fluid dynamics applications in bio-engineering, are very often defined by multiple dynamical or time-dependent in-/outflow and mix-in-/outflow (coexistence of local forward and reverse flows at a single in-/outlet surface) boundaries with complex geometries [1]. Since determining the cross-section velocity profile at these boundaries is much more difficult than measuring the boundary pressure as the latter is merely time-dependent and can be considered as constant along the entire cross-section surface, imposing pressure, other than velocity, boundary conditions is often preferred in hemodynamic flow simulations. For grid-based methods, despite the implementation of dynamical pressure boundary conditions is well-established, its employment for practical hemodynamic problems is often very difficult because of the intrinsic limitation on modeling the associated complex fluid-structure interaction (FSI), especially when mesh topological changes are involved. On the other hand, although the meshfree SPH (smoothed particle hydrodynamics) method is free of mesh topologies and able to model complex FSI problems effectively under a unified computational framework [2, 3, 4], it has not been widely employed for hemodynamic flow simulations due to the remaining well-known challenge of pressure boundary conditions.

In the most popular weakly compressible SPH (WCSPH) method, since the velocity field and pressure are not directly coupled due to the approxi-

mation of incompressible condition, a straightforward approach by which the particle velocity at the boundary can be updated from given pressure condition directly is yet to be developed. Holmes et al. [5] obtains the boundary particle velocity from a given constant pressure at simple planer in-/outflow boundaries indirectly through an elaborate correction involving the continuity equation and the artificial equation of state. It is still unclear whether this approach can be effectively employed for practical cases with dynamical pressure, mix-in-/outflow boundaries of complex geometries.

While the decoupling between particle pressure and velocity is not the case for incompressible SPH (ISPH) method, the implementation for general pressure boundary condition is still troublesome due to the ineffectiveness of particle handling, such as populating ghost particles, generating and deleting fluid particles at in-/outlets. For example, Hirschler et al. [6] and Kunz et al. [7] employed a mirror-axes particle technique to generate ghost and fluid particles for specifying constant pressure at simple domain boundaries. However, no matter using fixed or moving axes, significant numerical errors characterized by the artifacts of void regions and disorder particles are produced at the in-/outlets. In comparison, Monteleone et al. [8] developed a grid-based approach for generating ghost particles and a very complex geometric method using conical scan to generate inflow fluid particles at the in-/outlets. Together with further elaborative modifications on the coefficient matrix and the right-hand-side term of the pressure Poisson equation, the method is able to avoid the artifacts produced in Ref. [6, 7].

In this paper, we develop a dynamical pressure boundary condition for WCSPH to simulate hemodynamic flow with in-/outlets with general com-

plex geometries. With the assumption of zeroth-order consistency in SPH discretization, the present dynamic boundary pressure is imposed directly to compute the near-boundary gradient and to circumvent the cumbersome handling of ghost particles as in previous work. Different from Ref. [5], the present particle velocity at the boundary is obtained straightforwardly from the discretized momentum conservation equation. Also different from Ref. [8], the present meshfree method does not rely on grid-based approach but a bidirectional buffer for particle handling, i.e. generating and deleting fluid particles at the in-/outlets. Although the present particle handling is quite simple, it does not produce artifacts as in Refs. [6, 7]. Note that, the buffer used in this paper is relevant to those in several other SPH boundary conditions, such as periodic [9, 10, 11], open [12, 13, 14, 15, 16, 17, 18] and free-stream [19] conditions. The difference is that the present buffer, at the first time, is able to cope with the mix-in-/outflow, where particle generation and deletion are carried out at a single boundary surface, helped by periodically relabelling buffer particles at each time step.

The remainder of this paper is organized as follows. First, Section 2 gives a brief overview of the underlying WCSPH method. In Section 3, the proposed dynamical pressure boundary condition is detailed. The accuracy, convergence and applicability of the developed method are demonstrated by several flow examples in Section 4, including the startup of Poiseuille and Hagen-Poiseuille flows, PIVO (Pressurized Inlet, Velocity Outlet) and VIPO (Velocity Inlet, Pressure Outlet) channel flows, pulsatile channel flow, and generic carotid and aorta flows coupling with Windkessel model for the dynamical boundary pressure. Finally, concluding remarks are given in Section 5. The

code accompanying this work is implemented in the open-source SPHinXsys library [4], and is available at the project website <https://www.sphinxsys.org> and the corresponding Github repository.

2. Weakly-compressible SPH method

2.1. Governing equations

Within the Lagrangian framework, the mass- and momentum-conservation equations are respectively written as

$$\frac{d\rho}{dt} = -\rho \nabla \cdot \mathbf{v}, \quad (1)$$

and

$$\frac{d\mathbf{v}}{dt} = -\frac{1}{\rho} \nabla p + \nu \nabla^2 \mathbf{v}, \quad (2)$$

where ρ is the density, t the time, \mathbf{v} the velocity, p the pressure, and ν the kinematic viscosity. Under the weakly-compressible assumption, the system of Eqs.(1) and (2) are closed by the artificial isothermal equation of state (EoS)

$$p = c_0^2(\rho - \rho_0), \quad (3)$$

where $c_0 = \lambda U_{max}$ represents the artificial sound speed with U_{max} indicating the maximum anticipated flow speed, and ρ_0 the initial reference density. In WCSPH method, sufficiently large coefficient λ is selected to ensure near incompressible behavior [5, 20, 21].

2.2. SPH discretization

Following Refs.[4, 22, 23, 24, 25], both the mass- and momentum-conservation equations Eqs.(1) and (2) are discretized using the Riemann-based SPH scheme, in respect to particle i

$$\frac{d\rho_i}{dt} = 2\rho_i \sum_j \frac{m_j}{\rho_j} (\mathbf{v}_i - \mathbf{v}_{ij}^*) \cdot \nabla W_{ij}, \quad (4)$$

and

$$\frac{d\mathbf{v}_i}{dt} = -2 \sum_j m_j \left(\frac{P_{ij}^*}{\rho_i \rho_j} \right) \nabla W_{ij} + 2 \sum_j m_j \frac{\eta \mathbf{v}_{ij}}{\rho_i \rho_j r_{ij}} \frac{\partial W_{ij}}{\partial r_{ij}}, \quad (5)$$

where m is the particle mass, η the dynamic viscosity, subscript j the neighbor particles, and $\mathbf{v}_{ij} = \mathbf{v}_i - \mathbf{v}_j$ the relative velocity between particles i and j . Also, ∇W_{ij} denotes the gradient of the kernel function $W(|\mathbf{r}_{ij}|, h)$, where $\mathbf{r}_{ij} = \mathbf{r}_i - \mathbf{r}_j$, and h the smooth length. Furthermore, $\mathbf{v}_{ij}^* = U_{ij}^* \mathbf{e}_{ij} + (\bar{\mathbf{v}}_{ij} - \bar{U}_{ij} \mathbf{e}_{ij})$ with $\mathbf{e}_{ij} = \mathbf{r}_{ij}/r_{ij}$, $\bar{\mathbf{v}}_{ij} = (\mathbf{v}_i + \mathbf{v}_j)/2$ the average velocity between particles i and j and $\bar{U}_{ij} = \bar{\mathbf{v}}_{ij} \cdot \mathbf{e}_{ij}$. Here, P_{ij}^* and U_{ij}^* are obtained by solving the inter-particle one-dimensional Riemann problem with a low dissipation limiter as given by Ref. [26].

In order to increase the computational efficiency, the dual-criteria time stepping method [24] is employed here. Therefore, the particle cell-linked lists and neighbor configurations are only rebuilt for each advection time step (referred to as time step herein) and kept unchanged for the several acoustic time-steps. One can refer Ref. [24] details. In addition, to decrease the accumulated density error during long-term simulations, a density initialization scheme [4] is also used to stabilize the density field prior the acoustic time

steps as

$$\rho_i = \rho_0 \frac{\sum W_{ij}}{\sum W_{ij}^0}, \quad (6)$$

where the superscript 0 represents the reference value in the initial configuration.

2.3. Transport-velocity formulation

To avoid particle clumping and void regions in SPH simulations where the tensile instability is present [27, 28], regularization is implemented to maintain a uniform particle distribution [29, 30]. Currently, the particle shifting technique (PST) [27, 28, 30, 31, 32, 33] and the transport-velocity formulation (TVF) [23, 34] are two typical schemes to address this issue. In the present work, the TVF scheme is adopted, and the particle advection velocity $\tilde{\mathbf{v}}$ is rewritten as

$$\tilde{\mathbf{v}}_i(t + \delta t) = \mathbf{v}_i(t) + \delta t \left(\frac{d\mathbf{v}_i}{dt} - p_{max} \sum_j \frac{2m_j}{\rho_i \rho_j} \frac{\partial W_{ij}}{\partial r_{ij}} \mathbf{e}_{ij} \right), \quad (7)$$

where the global background pressure $p_{max} = 7\rho_0 \mathbf{v}_{max}^2$ with \mathbf{v}_{max} denoting the maximum particle velocity at each time step [24].

Since the TVF scheme is applicable only to inner fluid particles far away from in-/outlet boundaries [34], accurately identifying boundary particles is a necessary prior. To avoid misidentifying and missing boundary particles [19, 35, 36, 37], the spatio-temporal identification approach [19] is utilized in present work, where approximately three layers of fluid particles are identified as boundary particles.

3. Dynamical pressure boundary condition

3.1. Bidirectional in-/outflow buffer

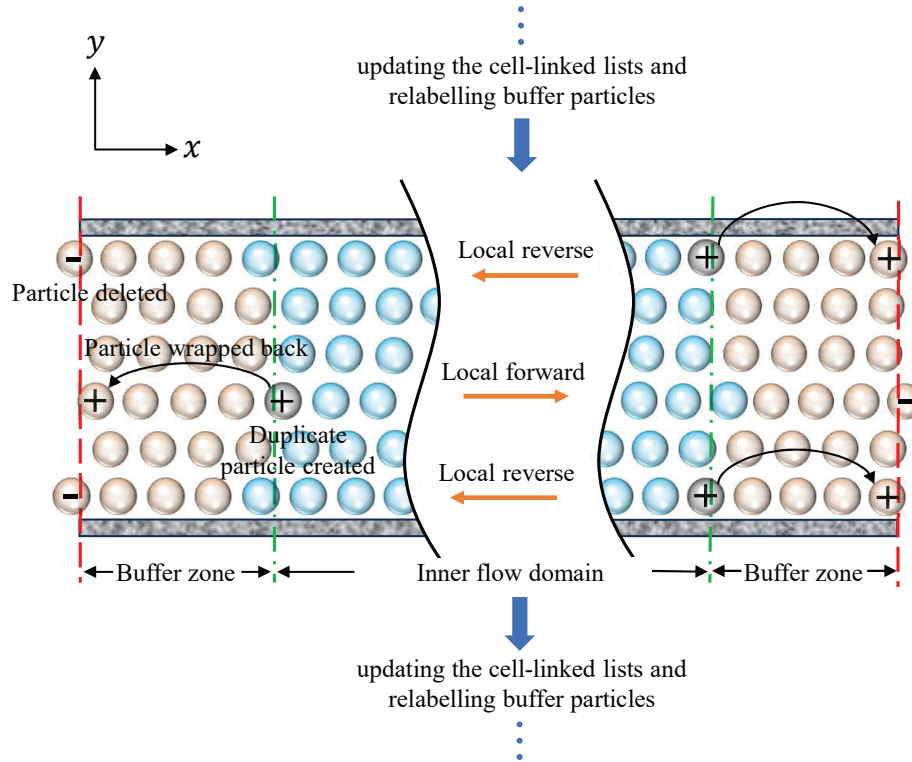


Figure 1: The illustration of particle handling for the bidirectional in-/outflow buffer. Within the left and right buffers, the dashed red lines indicate the in-/outlet bound, and the dot-dashed green lines connect the buffers to the inner flow domain. The inner-domain, buffer and duplicate particles are colored with blue, gold and gray, respectively. Note that, the wall end should be aligned to the buffer surface.

In Figure 1, a two-dimensional bidirectional flow along x -axis between two parallel walls is sketched to demonstrate the particle handling of the bidirectional in-/outflow buffer. To realize the bidirectional buffer, the key step is to relabel buffer particles (indicating the fluid particles located within the buffer zone) at the end of each time step. For example, buffer and inner-

domain particles are assigned the integer labels 1 and 0, respectively. Note that, as the present smoothing length $h = 1.3dp$, with dp denoting the initial particle spacing, is used, the buffer should consist of at least three layers of particles to ensure full support for the inner-domain particles next to the buffer.

Here, since the right buffer operates based on the same principle, only the left buffer in Figure 1 is used to detail the present method. For a local forward flow at the present time step, as shown in Figure 1, the buffer will generate new particles. In this case, some buffer particles cross the right buffer bound. Duplicate particles are generated with the same states as the crossing ones, and then treated as ordinary particles of the inner flow domain. Meanwhile, the original buffer particles will be recycled from the left buffer bound at the periodic positions [17, 19]. Correspondingly, if the buffer particles leave the left buffer bound in a local reverse flow, as shown in Figure 1, they will be deleted as outflow particles. Since some fluid particles from inner domain may enter the buffer zone from the right buffer bound at the present time step, all fluid particles within the buffer zone will be relabeled at the end of present time step (after the cell-linked lists have been rebuilt). Note that, this can be easily achieved by checking whether the particles in the nearby updated cell-linked lists are located within the buffer zone.

It is worthy to emphasize that the present bidirectional buffer copes with the mix-in-/outflow boundary in a natural way. At the right buffer bound, the inflow particles are created and the outflow particles are identified as new buffer particles at the end of time step. At the left buffer bound, while the inflow is handled by recycling the buffer particles leaving the right buffer

bound, the outflow particles are simply deleted. Figure 2 gives typical mix-in-/outflow profile obtained by the present method.

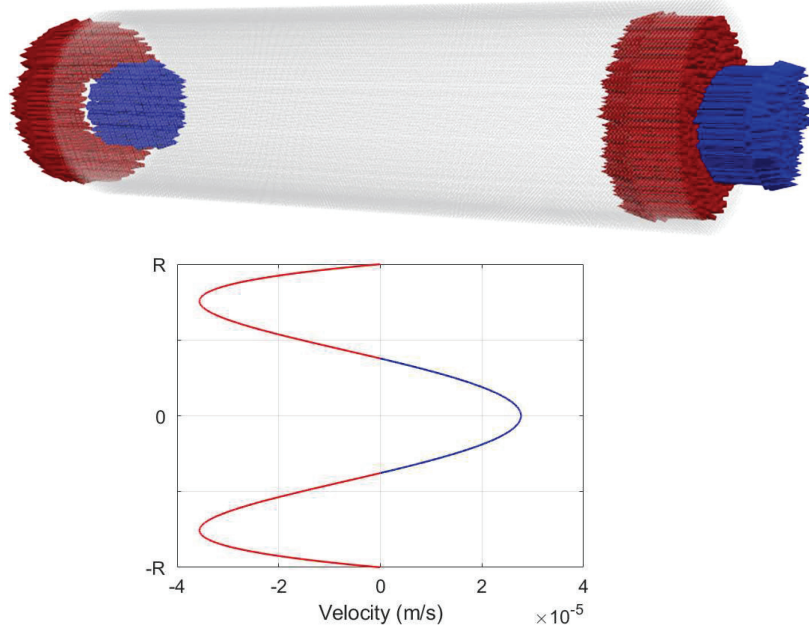


Figure 2: Velocity profile with mixed forward and reverse flows at the in-/outlet boundary (top panel), corresponding to the analytical velocity profile (bottom panel) at $t = 7.975s$ of the pulsatile flow in Subsection 4.4. The velocity vector in top panel is scaled to a uniform length, with the flow direction indicated by the arrow.

3.2. Imposing dynamical boundary pressure

As shown in Figure 3, the support domain of fluid particles near the in-/outlet (also referred to as near-boundary particles herein) is truncated, with the postulated "missing" particles beyond the buffer bound. For pressure boundary condition, the given boundary pressure p_{target} needs to be specified as the evolution of the in-/outflow velocity is strongly influenced by the corresponding near-boundary pressure gradient.

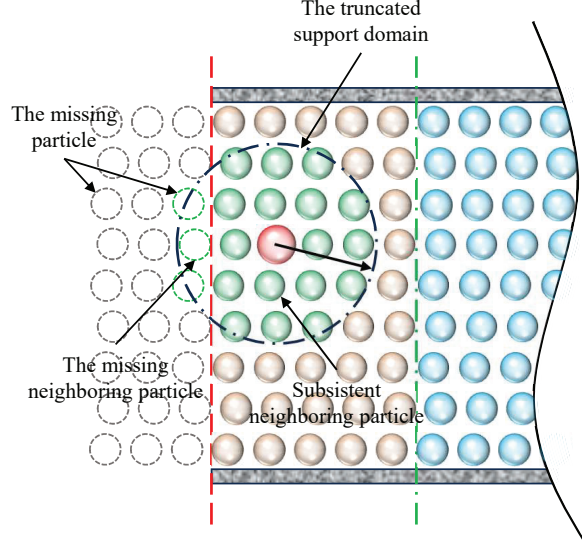


Figure 3: The truncated support domain of fluid particles near the in-/outlet.

For a particle with full kernel support, the standard SPH discretization of gradient [38] approximates the zeroth-order consistent, i.e., $\sum_j \frac{m_j}{\rho_j} \nabla W_{ij} \approx \mathbf{0}$. In this paper, this property is utilized to approximate pressure gradient for a near-boundary particle. Specifically, a near-boundary particle i has

$$\sum_j \frac{m_j}{\rho_j} \nabla W_{ij} + \sum_k \frac{m_k}{\rho_k} \nabla W_{ik} \approx \mathbf{0}, \quad (8)$$

with j and k represent the subsistent and "missing" neighboring particles, respectively. Referring Eq. (5), the SPH approximation of the pressure gradient at a near-boundary particle can be written as

$$\nabla p_i = 2 \sum_j P_{ij}^* \frac{m_j}{\rho_j} \nabla W_{ij} + 2 \sum_k P_{ik}^* \frac{m_k}{\rho_k} \nabla W_{ik}. \quad (9)$$

By using Eq.(8) and assuming uniform in-/outlet pressure as $p_{target} = P_{ik}^*$,

Eq. (9) can be rewritten as

$$\nabla p_i = 2 \sum_j P_{ij}^* \frac{m_j}{\rho_j} \nabla W_{ij} - 2p_{target} \sum_j \frac{m_j}{\rho_j} \nabla W_{ij}. \quad (10)$$

Then, the modified Eq. (5) for near-boundary particles has the form

$$\begin{aligned} \frac{d\mathbf{v}_i}{dt} = & -2 \sum_j m_j \left(\frac{P_{ij}^*}{\rho_i \rho_j} \right) \nabla W_{ij} + 2p_{target} \sum_j \left(\frac{m_j}{\rho_i \rho_j} \right) \nabla W_{ij} \\ & + 2 \sum_j m_j \frac{\eta \mathbf{v}_{ij}}{\rho_i \rho_j r_{ij}} \frac{\partial W_{ij}}{\partial r_{ij}}. \end{aligned} \quad (11)$$

Note that, the present formulation does not require ghost particles to replace the postulate "missing" particle as in previous work. Furthermore, as the second term on the right side of Eq. (11) vanishes for particles with full kernel support, Eq. (11) is applied to all buffer particles in present work, without specifically identifying near-boundary particles with truncated kernel support. Also note that, the velocity updated by Eq.(11) should be perpendicular to the in-/outlet boundary, aligning with the in-/outflow condition [5]

$$\mathbf{v}_i = (\mathbf{v}_i \cdot \hat{u}) \hat{u}, \quad (12)$$

where \hat{u} is the unit normal vector of the in-/outlet boundary or buffer bound.

To cope with the truncation for density summation, the reinitialization of Eq. (6) is not carried out for near-boundary particles (i.e., buffer particles herein), and the density of the newly populated (actually recycled) particles in the bidirectional in-/outflow buffer is obtained following the boundary

pressure and EoS as

$$\rho_i = \rho_0 + p_{target}/c_0^2. \quad (13)$$

When the bidirectional in-/outlet buffer works with the velocity in-/outflow boundary condition, such as in PIVO (Pressurized Inlet, Velocity Outlet) and VIPO (Velocity Inlet, Pressure Outlet) flows, the pressure boundary condition should also be imposed at the velocity in-/outlet to eliminate the truncated error in approximating pressure gradient, but the corresponding p_{target} in Eq.(11) is given as p_i . Meanwhile, both the density and pressure of newly populated particles remain unchanged.

4. Numerical examples

In this section, to validate the present method, a set of benchmark cases are simulated and the results are compared with those of previous experiments and simulations. These cases including the startup of Poiseuille and Hagen-Poiseuille flows, PIVO and VIPO channel flows, and carotid and aorta flows coupling with Windkessel model for the dynamical boundary pressure. The 5th-order Wendland kernel [39] is employed in all the following simulations. As for the treatment of wall boundary, a one-sided Riemann solver is employed and we refer to Ref. [26] for more details.

4.1. Startup of Poiseuille flow

As a well-defined benchmark to verify the pressure boundary condition, the startup of two-dimensional Poiseuille flow [5, 21, 40, 41, 42] is studied herein. The analytical velocity evolution $\mathbf{v}_x(y, t)$ is given as

$$\begin{aligned}
\mathbf{v}_x(y, t) &= \frac{\Delta P}{2\eta L}y(y - d) \\
&+ \sum_{n=0}^{\infty} \frac{4\Delta P d^2}{\eta L \pi^3 (2n + 1)^3} \sin\left(\frac{\pi y}{d}(2n, \right. \\
&\left. + 1)\right) \exp\left(-\frac{(2n + 1)^2 \pi^2 \eta}{\rho d^2}t\right)
\end{aligned} \tag{14}$$

where $y \in (0, d)$ with d denoting the distance between plates, and ΔP the pressure drop across a flow length of L . Figure 4 shows the schematic of simulation setup. A flow with the domain size $L = 0.004m$ and $d = 0.001m$ is driven by a inlet and outlet pressure of $0.2Pa$ and $0.1Pa$, respectively, for a constant pressure difference of $\Delta P = 0.1Pa$. In this simple unidirectional flow, the bidirectional buffers is only used for particle generation at the inlet, and deletion at the outlet. The dynamic viscosity is set as $\eta = \sqrt{\rho d^3 \Delta P / 8 L Re}$ with the fluid density $\rho = 1000kg/m^3$ and the Reynolds number $Re = 50$. The fluid and solid-wall particles are initialized on the Cartesian Lattice with a uniform particle spacing of $dp = d/50$. Note that, the artificial sound speed c_0 is chosen here with a large value as $100\mathbf{v}_x^{max}$, with $\mathbf{v}_x^{max} = d^2 \Delta P / 8 \eta L$, to ensure that the fast startup response is captured accurately by the weakly compressible model.

In Figure 5, velocity profiles at 5 instants are extracted and compared with their corresponding analytical solutions. Throughout the flow development process, the obtained velocity profiles consistently exhibit a parabolic shape that closely aligns with the analytical solution. The maximum velocity occurs at the centerline, and the velocity approaches zero near the plates as the no-slip solid-wall boundary condition [43] is applied. Following the work of

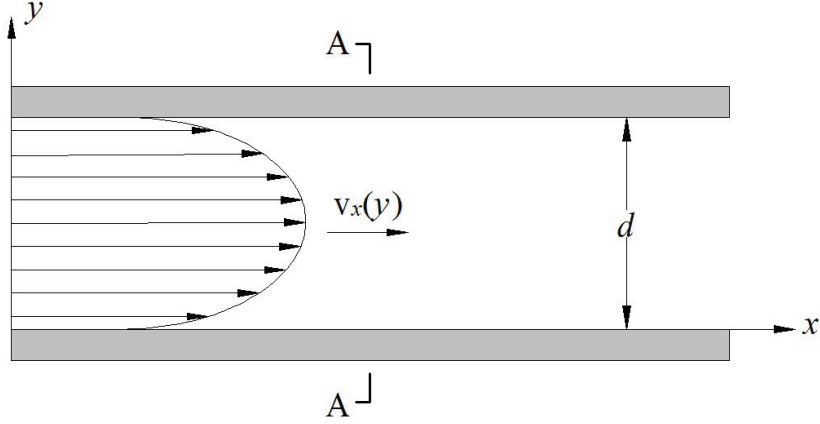


Figure 4: Schematic of Poiseuille flow. Velocity profile is extracted at the cross-section A in the simulation.

Holmes et al. [5], an accuracy measurement is also carried out with the Root Mean Square Error Percentage (RMSEP) over the whole velocity profile

$$RMSEP = \sqrt{\frac{1}{N} \sum_{n=1}^N \left(\frac{\mathbf{v}_x(y_n, t) - \tilde{\mathbf{v}}_x(y_n, t)}{\mathbf{v}_x(y_n, t)} \right)^2}, \quad (15)$$

where N is the number of measuring points at a given time t , $\mathbf{v}_x(y_n, t)$ and $\tilde{\mathbf{v}}_x(y_n, t)$ the analytical and numerical velocities, respectively. The largest error of 1.81% occurs at the start-up time $t = 0.1s$, while errors at other instants are around 1%, implying good agreement with the analytical solution.

4.2. Startup of Hagen-Poiseuille flow

To further verify the effectiveness of the proposed dynamical pressure boundary condition in 3-D case, the startup of Hagen-Poiseuille flow, which is the direct analogue to the Poiseuille flow in a circular pipe, is studied here, while all other physical and geometrical parameters remain unchanged. The analytical velocity evolution $\mathbf{v}_x(r, t)$ is given as

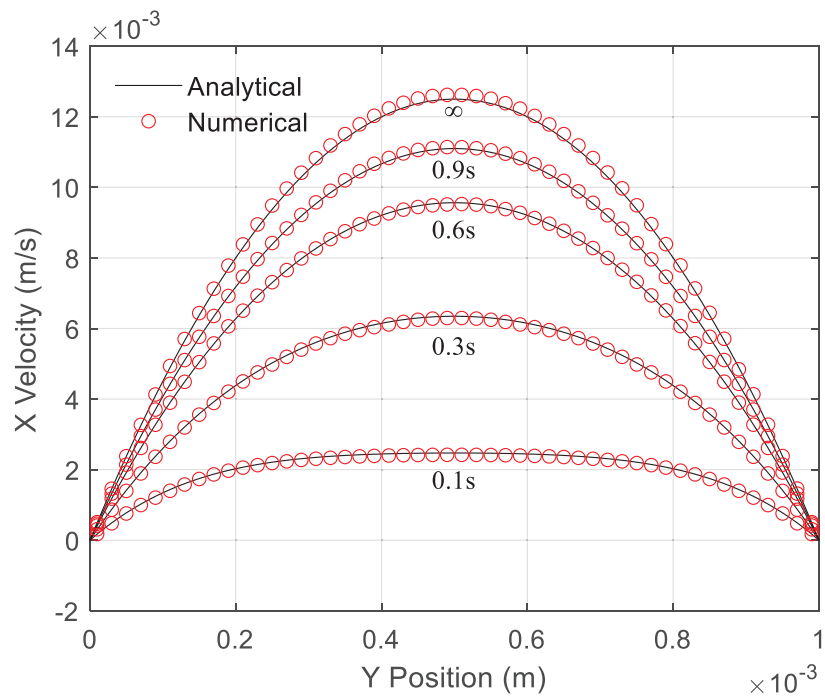


Figure 5: Comparison of numerical and analytical velocity profiles at 5 instants of the Poiseuille flow. The errors at 5 instants, from $t = 0.1s$ to ∞ , are 1.81%, 0.95%, 0.67%, 0.86% and 1.22%, respectively.

$$\mathbf{v}_x(r, t) = \frac{\Delta P}{4\eta L}(R^2 - r^2) - \sum_{n=1}^{\infty} \frac{\Delta P R^2}{\eta L \alpha_n^2} \frac{J_2(\alpha_n)}{J_1^2(\alpha_n)} J_0\left(\frac{r\alpha_n}{R}\right) \exp\left(-\frac{\eta \alpha_n^2}{\rho R^2} t\right), \quad (16)$$

where $r \in (0, R)$ with $R = d/2$ denoting the pipe radius. Here J_n ($n = 0, 1, 2$) are the Bessel functions of the first kind, and α_n ($n = 1, 2, \dots$) are the roots of J_0 . The dynamic viscosity $\eta = \sqrt{\rho R^2 \Delta P / 4Re}$ and, similarly, a large artificial sound speed $c_0 = 100 \mathbf{v}_x^{max}$ with $\mathbf{v}_x^{max} = R^2 \Delta P / 4\eta L$ are applied.

Figure 6 illustrates a comparison between numerical and analytical velocity profiles at 6 instants. The fluid velocity varies along the radial direction, with the maximum velocity occurring at the centerline and progressively decreasing towards the pipe's wall, which also follows the parabolic velocity profile. Furthermore, similar with the 2-D Poiseuille flow, the largest RMSEP, approximately 2.97%, occurs at the start-up time $t = 0.03s$, and the error gradually diminishes to within 1% over time. This error range also demonstrates a good agreement with the analytical solution in the 3-D case.

Referring to the convergence study on the Hagen-Poiseuille flow conducted by Holmes et al. [5], the accuracy and convergence of the present dynamical pressure boundary condition are also investigated with varying spatial resolution herein. Figure 7 illustrates the RMSEP across the entire velocity profile at time $t = \infty$ for various particle resolutions. As the number of particles spanning the circular pipe, i.e. $2R/dp$, exceeds 30, the errors reach a saturation regime and are sufficiently small (around 1%) compared to the analytical solution. This level of accuracy and convergence closely aligns with that found in the study by Holmes et al. [5].

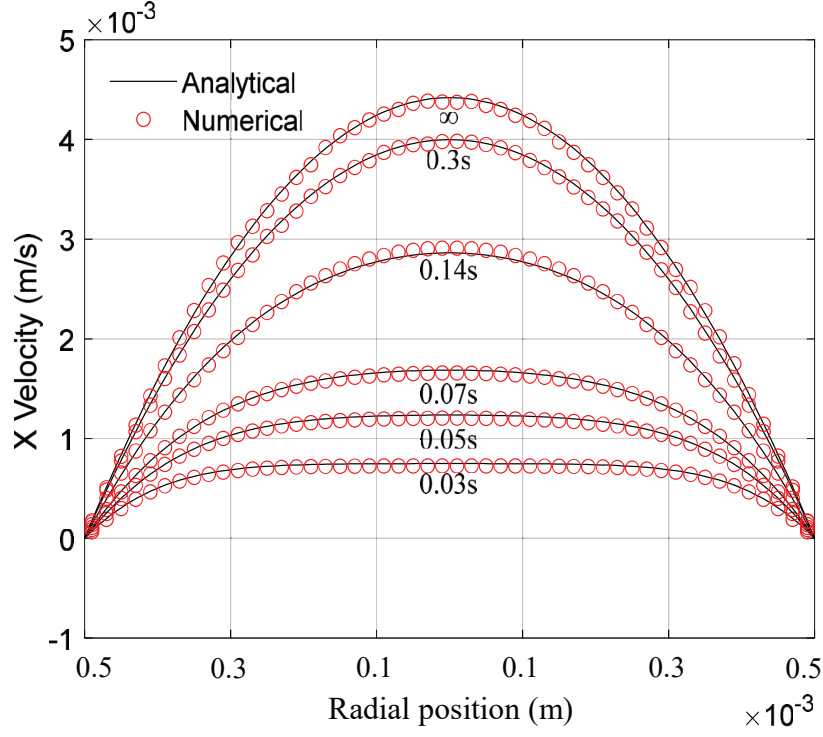


Figure 6: Comparison of numerical and analytical velocity profiles at 6 instants of the Hagen-Poiseuille flow. The errors at 6 instants, from $t = 0.03s$ to ∞ , are 2.97%, 1.88%, 1.61%, 1.5%, 0.74% and 0.89%, respectively.

4.3. PIVO and VIPO channel flows

As the setups of PIVO and VIPO are commonly utilized in practical simulations, both PIVO and VIPO channel flows are considered here. Based on the Poiseuille flow setup in Sec. 4.1, the pressure in-/outflow boundary conditions are replaced by the velocity boundary condition in turn, and the prescribed velocity profile is analytically determined by Eq. (14) at time $t = \infty$.

According to the setup parameters, the pressure difference between the inlet and outlet should remain constant at $\Delta P = 0.1Pa$. In detail, in PIVO

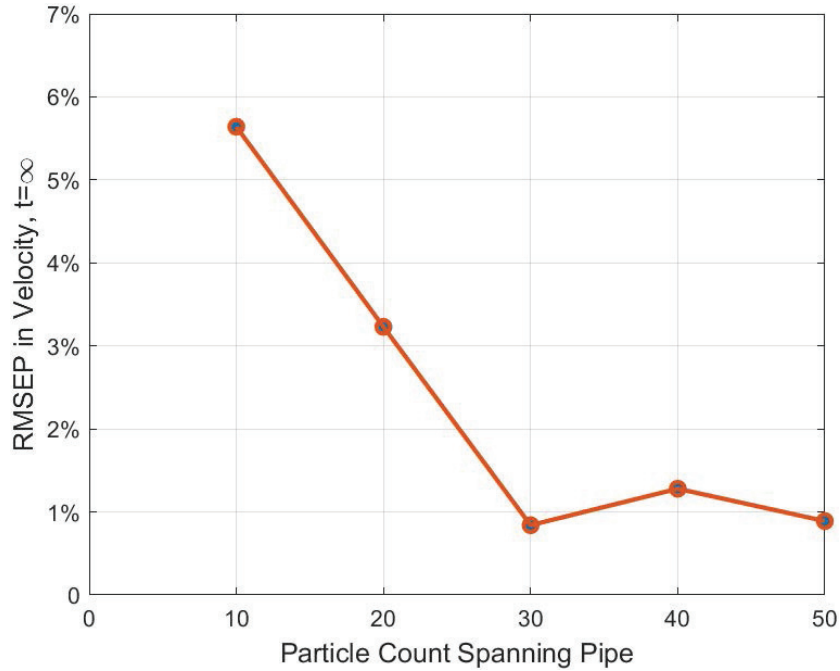


Figure 7: Plot of RMSEP for the whole velocity profile at time $t = \infty$ for Hagen-Poiseuille flow at different particle resolutions.

flow, the predicted boundary pressure at the velocity outlet should be kept at $0.1Pa$, while in VIPO flow, the predicted boundary pressure at the velocity inlet should be kept at $0.2Pa$. Figure 8 gives the pressure distributions for both flows and it is observed that the results are aligning well with the theoretical expectations. Figure 9 compares the computed velocity profiles of both PIVO and VIPO channel flows with the corresponding analytical solution and obtained small errors of 1.07% and 2.32% respectively, indicating again good agreement with the analytical solution.

4.4. Pulsatile channel flow

The dual functionality of the bidirectional in-/outflow buffer, serving for both particle generation and deletion, is specifically validated here through

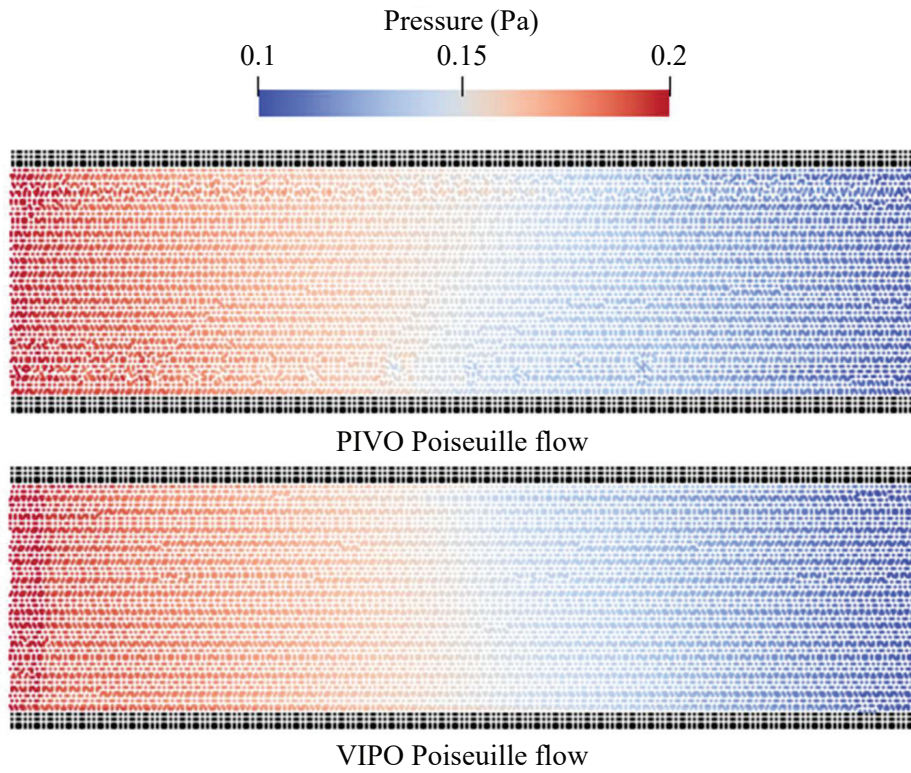


Figure 8: Pressure contours of PIVO (top panel) and VIPO (bottom panel) channel flows. For both cases, the left and right boundaries are the inlet and outlet, respectively.

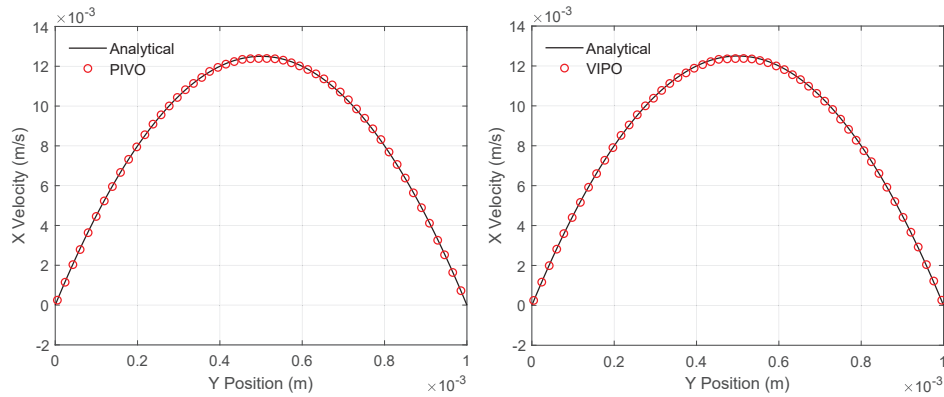


Figure 9: Comparison of numerical and analytical velocity profiles of PIVO (left panel) and VIPO (right panel) channel flows. The errors for PIVO and VIPO channel flows are 1.07% and 2.32%, respectively.

a pulsatile channel flow. To be more specific, building upon the Hagen-Poiseuille flow model discussed in Subsection 4.2, its constant pressure gradient is modified to follow a cosine function over time, i.e., $P' = \Delta P/L = 0.1 \cos(t)/0.004 = 25 \cos(t)$, as illustrated in the upper panel of Figure 10. The pulsatile flow profile was first derived by John R. Womersley for studying the blood flow in arteries [44], and the analytical solution is given as

$$\mathbf{v}_x(r, t) = \mathbf{Re} \left\{ \sum_{n=0}^N \frac{iP'_n}{\rho n \omega} \left[1 - \frac{J_0(\alpha n^{\frac{1}{2}} i^{\frac{3}{2}} \frac{r}{R})}{J_0(\alpha n^{\frac{1}{2}} i^{\frac{3}{2}})} \right] e^{in\omega t} \right\}, \quad (17)$$

where $r \in (0, R)$, $\alpha = R\sqrt{\omega\rho/\eta}$ the dimensionless Womersley number, ω the angular frequency of the first harmonic of a Fourier series of an oscillatory pressure gradient, P'_n the pressure gradient magnitude for the frequency $n\omega$, $J_0(\cdot)$ the Bessel function of first kind and order zero, i the imaginary number, and $\mathbf{Re}\{\cdot\}$ the real part of a complex number.

It's well-known that the shape of the pulsatile flow profile changes depending on the Womersley number α . For example, a flattened velocity profile for $\alpha \gtrsim 2$ and a parabolic profile for $\alpha \lesssim 2$. In the present pulsatile flow with $\alpha = 0.8409$, suggesting viscous forces dominate the flow and resulting in a quasi-static pulse with a parabolic profile. Moreover, the time evolution of the velocity profile exhibits periodicity in both velocity magnitude and direction, which is consistent with the cosine-varying pressure gradient. In the lower panel of Figure 10, during one period from $t = 2\pi$ to 4π , the obtained velocity profiles extracted at 13 instants accurately follow the periodically evolving parabolic shape. In more detail, the parabolic velocity profile maintains a forward flow direction during the first quarter, but with a decreasing

magnitude over time. At $t = 2.5\pi$, the flow direction reverses, and the flow gradually accelerates until it reaches the maximum velocity at $t = 3\pi$. In the latter half of the period, this flow behavior will repeat, but with the opposite evolution of flow direction.

In the accuracy measurement using RMSEP, the numerical results also exhibit a good fit with their corresponding analytical solutions, with an overall error of approximately 3% for all 13 instants. For the objectives of this study, this level of accuracy is considered acceptable.

4.5. Generic carotid and aorta flows

To investigate the applicability and versatility of the present dynamical pressure boundary condition for hemodynamic simulations, flow simulations are preliminarily conducted on carotid and aorta structures, as shown in Figure 11. The blood is modeled as Newtonian fluid with density of 1060 kg/m^3 [45] and viscosity of $0.00355 \text{ Pa}\cdot\text{s}$ [46], and the vascular wall is simplified as a rigid body. At inlet, a velocity inflow boundary condition with a plug profile is implemented, while the pressure boundary condition is enforced across all outlets. Note that, to increase the computational efficiency, the standard choice of artificial sound speed $c_0 = 10U_{max}$ is applied [21].

For the carotid flow, considering the pulsatile nature of blood circulation, the inflow velocity is defined as a waveform function of time, with the flow direction aligned along the normal vector of the inlet boundary surface

$$\mathbf{v}_{inlet}(t) = \begin{cases} 0.5\sin[4\pi(t + 0.0160236)] & 0.5n < t \leq 0.5n + 0.218 \\ 0.1 & 0.5n + 0.218 < t \leq 0.5(n + 1) \end{cases}, \quad (18)$$

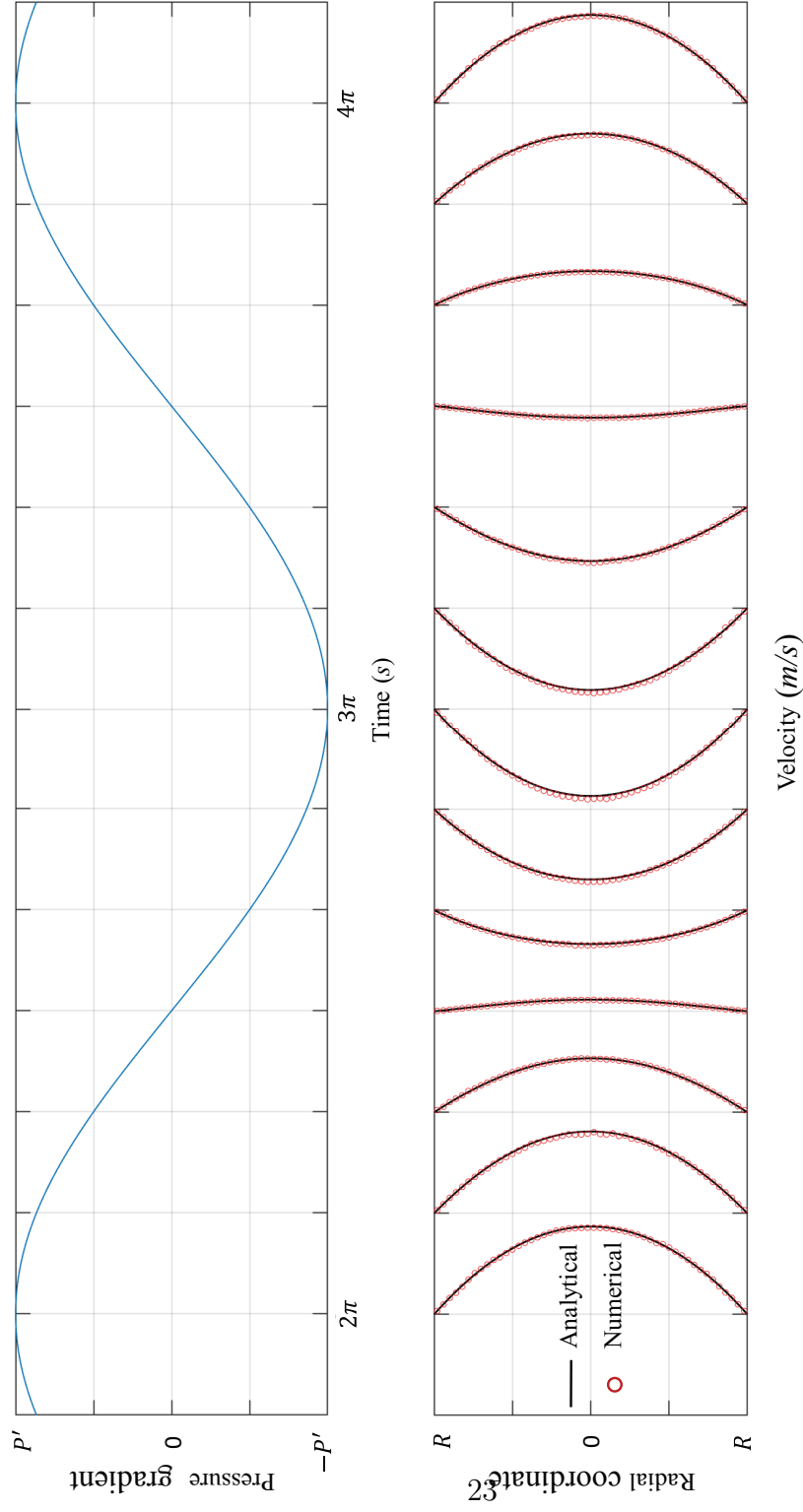


Figure 10: The pressure gradient as a cosine function (upper panel) in the Pulsatile flow, and the comparison (lower panel) of numerical and analytical velocity profiles at 13 indicative instants. The horizontal grid dimension in the lower panel spans a velocity range from 0 to $5.0E-3$ m/s. The errors at 13 instants, from $t = 2\pi$ to 4π , are 1.45%, 2.24%, 2.65%, 3.98%, 3.11%, 2.56%, 2.83%, 2.53%, 2.61%, 3.22%, 2.55%, 2.54% and 1.39%, respectively.

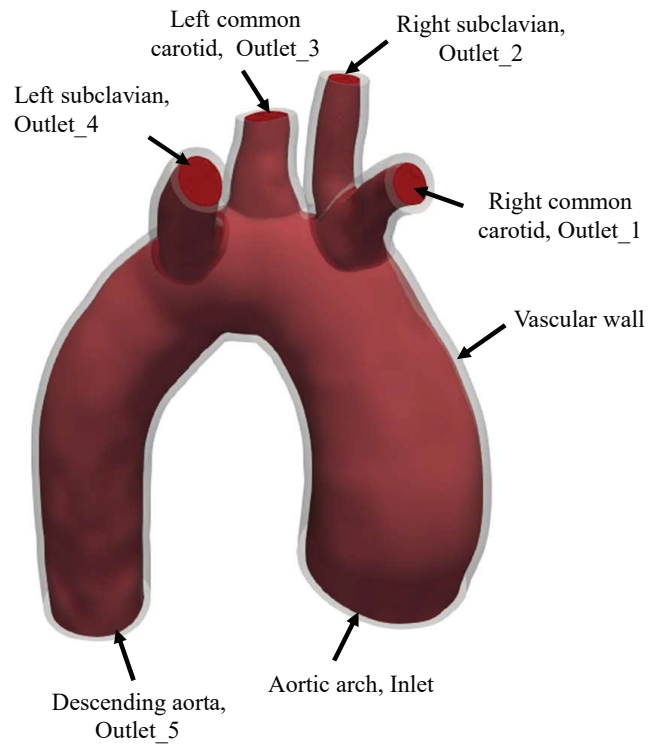
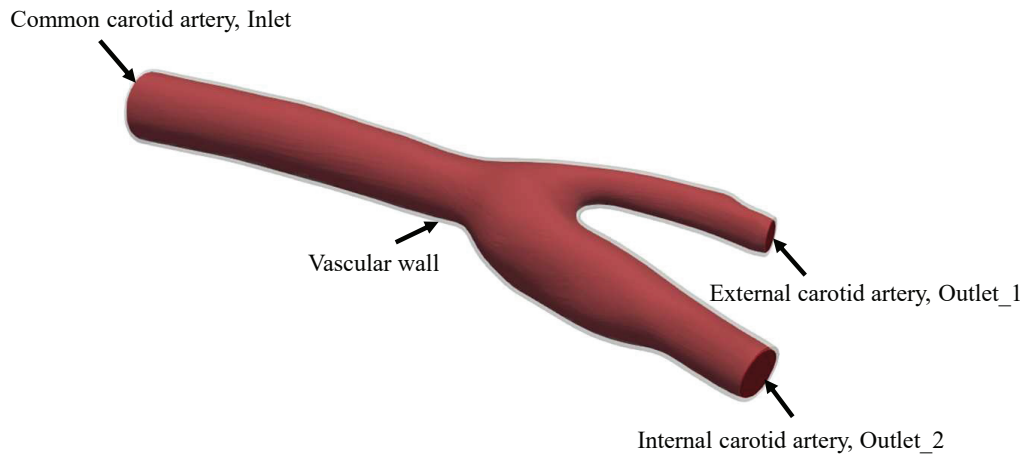


Figure 11: Schematic of the generic carotid and aorta flows.

where $n = 0, 1, 2, \dots$. Furthermore, because the blood pressure for a healthy person is around $120\text{mmHg}/80\text{mmHg}$ (systolic/diastolic), the constant average blood pressure 100mmHg is imposed at both outlets.

Figure 12 illustrates the velocity contours at 4 time instants during the 5th cycle. The blood flows into the bifurcation artery from the common carotid artery, and then the flow splits into the internal and external carotid arteries. Due to the geometric asymmetry of the blood vessel, the velocity magnitude and distribution in the internal and external carotid arteries are notably distinct. Moreover, the time-dependent pulsatile inflow also induces corresponding changes in the entire velocity field over time. To demonstrate the accuracy and reliability of the present simulation, especially for the pulsatile characteristic, the mass flow rate during the 5th cycle is chosen to be analyzed. In Figure 13, the time histories of both mass outflow rates correspond well to that of pulsatile mass inflow rate. Note that, due to the weakly compressible assumption in WCSPH method, mass flow rate fluctuates slightly in agreement with Ref. [5].

For the aorta flow, the waveform of inflow velocity in Figure 14 is approximated as Fourier series in term of time [47], which can mimic the continuous cardiac cycle of the waveform

$$\mathbf{v}_{inlet}(t) = a_0 + \sum_{n=1}^8 a_n \cos(nt\omega) + \sum_{n=1}^8 b_n \sin(nt\omega), \quad (19)$$

where the empirical variables for the Fourier series are listed in Table 1.

Different from the constant outlet pressure in the carotid flow, the outlet pressure $P(t)$ in the aorta flow is time-dependent and obtained by a 3-element

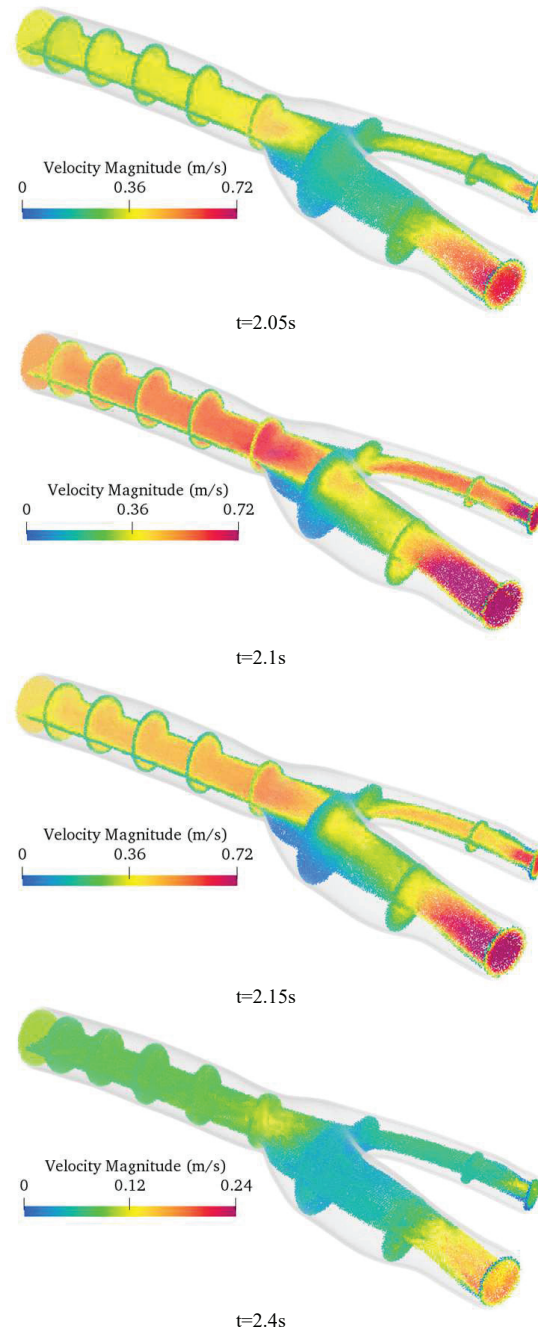


Figure 12: Velocity contours of carotid flow at 4 time instants of the 5th cycle. From top to bottom panels, the maximum velocities are around 0.72 m/s , 1.0 m/s , 0.86 m/s and 0.24 m/s , respectively.

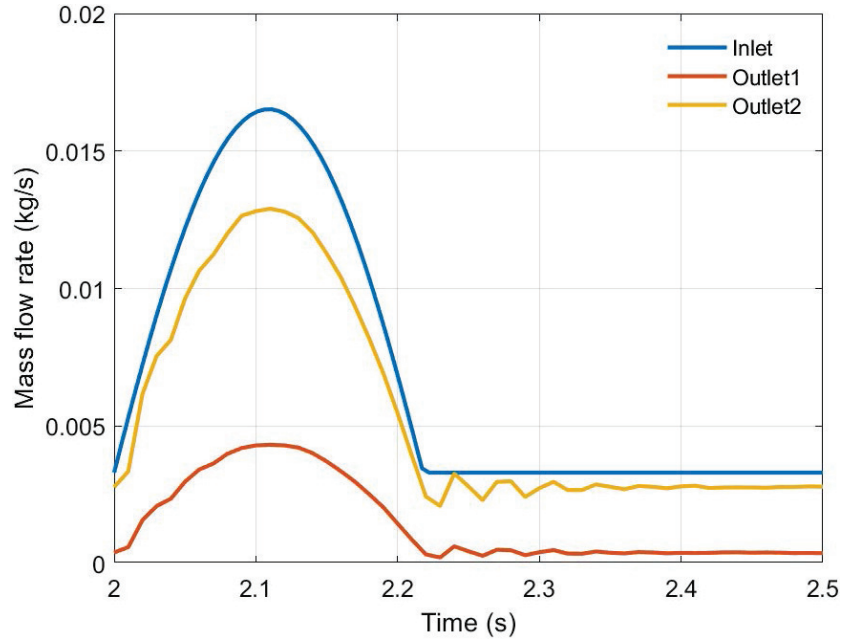


Figure 13: Time histories of mass in-/outflow rates in carotid flow. Both mass outflow rates are numerically measured, while the mass inflow rate is determined analytically.

Table 1: The empirical variables for the Fourier series [47]

Parameter	Value	Parameter	Value
a_0	0.3782	ω	8.302
a_1	-0.1812	b_1	-0.07725
a_2	0.1276	b_2	0.01466
a_3	-0.08981	b_3	0.04295
a_4	0.04347	b_4	-0.06679
a_5	-0.05412	b_5	0.05679
a_6	0.02642	b_6	-0.01878
a_7	0.008946	b_7	0.01869
a_8	-0.009005	b_7	-0.01888

(RCR) Windkessel model [1]

$$\left(1 + \frac{R_p}{R_d}\right)Q(t) + CR_p \frac{dQ(t)}{dt} = \frac{P(t)}{R_d} + C \frac{dP(t)}{dt}, \quad (20)$$

where $Q(t)$ is the blood flow volume, C the arterial compliance, R_p the characteristic resistance, and R_d the peripheral resistance. The values of Windkessel parameters [48, 49] used for the various daughter vessels are listed in Table 2.

Table 2: Parameters for the Windkessel outlet boundary conditions [48, 49]

Vessel	$R_p(\text{dynes } s/\text{cm}^5)$	$C(\text{cm}^5/\text{dynes})$	$R_d(\text{dynes } s/\text{cm}^5)$
Right common carotid	1180	7.70E-5	18400
Right subclavian	1040	8.74E-5	16300
Left common carotid	1180	7.70E-5	18400
Left subclavian	970	9.34E-5	15200
Descending aorta	188	4.82E-4	2950

Corresponding to the time history of inflow velocity over 7 cycles, Figure 14 shows the relative pressure at all outlets. Same as both analytical and numerical solutions for the blood pressure in Ref. [1], all the waveforms of the present outlet relative pressure exhibit a folding line shape, which is consistent with theoretical expectations. Note that, compared to the practical physiological scenario, the present inflow velocity, the Windkessel parameters of all daughter vessels, and the aorta geometry don't strictly match each other. Moreover, the corresponding physiological pressure data for the present aorta model are lacking. Hence, our primary focus is on the accuracy of the blood pressure waveform rather than the pressure magnitude. Figure 15 also illustrates the velocity contour and slices during the peak systole. In

the present plug-inlet boundary condition, the velocity peak isn't always at the center of the cross-section. Especially in the descending aorta, due to the inertia, the flow inside the curved vessel is pushed towards the outer side of the arch, which is in good agreement with the observations in Ref. [49].

5. Conclusion

In this paper, we develop a dynamical pressure boundary condition for the WCSPH method, characterizing a bidirectional in-/outflow buffer to simulate hemodynamic flows with complex geometric boundaries. With the assumption of zeroth-order consistency in the SPH discretization, the dynamical boundary pressure is imposed by the SPH approximation of the pressure gradient on near-boundary particles. The boundary pressure could be constant, time-dependent, or dynamically determined by the Windkessel model as in practical hemodynamic simulations. The bidirectional in-/outflow buffer is achieved by relabelling buffer particles at each time step, and is suitable for simulating both uni-/bidirectional flows, especially those with mixed in-/outflow boundary condition. The numerical results in 2-D and 3-D benchmark cases exhibit very good agreement with analytical solutions, demonstrating the accuracy and effectiveness of the present method. As the present method performs well in the generic carotid and aorta flow simulations, and thanks to the effectiveness of SPH method for FSI problems, our future focus will center on exploring cardiovascular hemodynamics and other relevant bio-engineering applications within a unified meshfree computational framework.

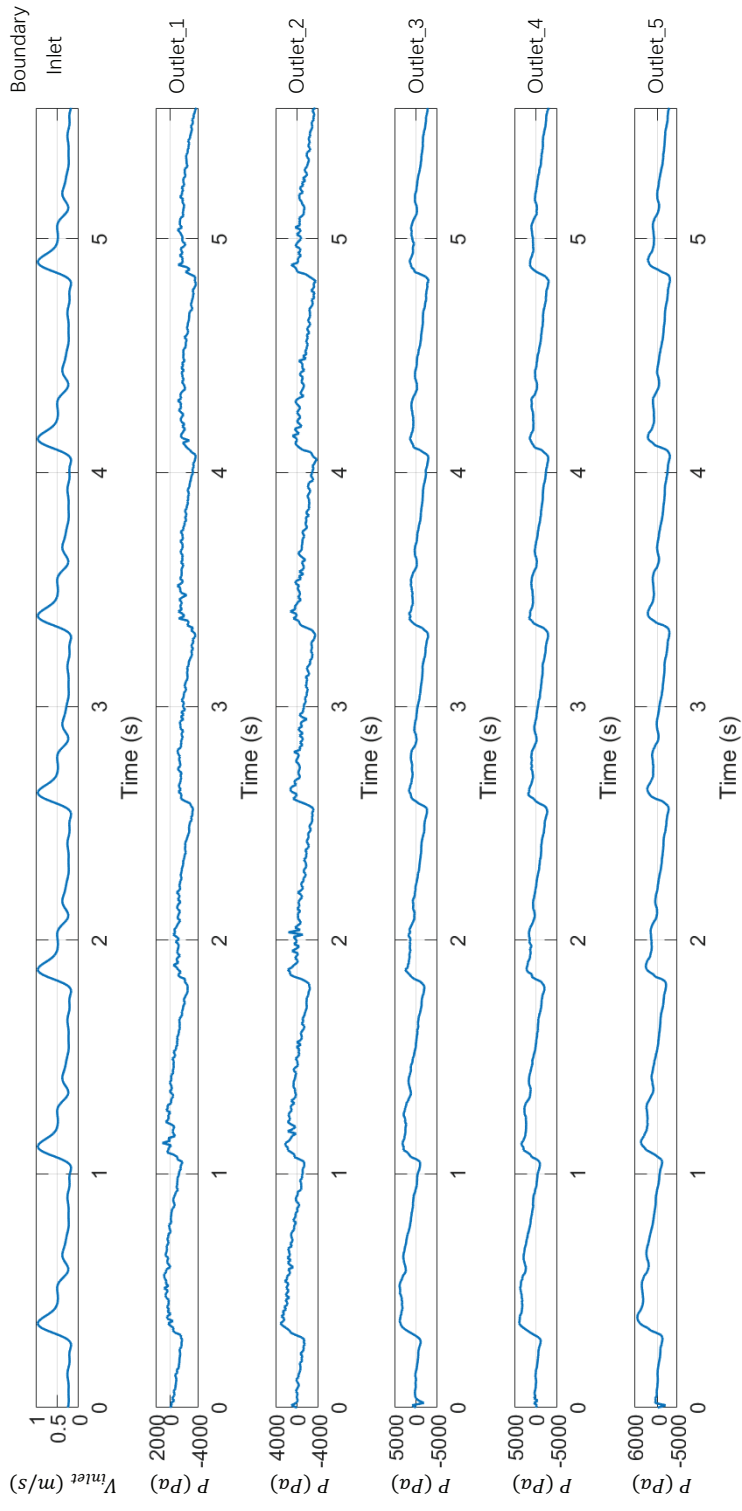


Figure 14: The time history of the inflow velocity and all outlet relative pressure.

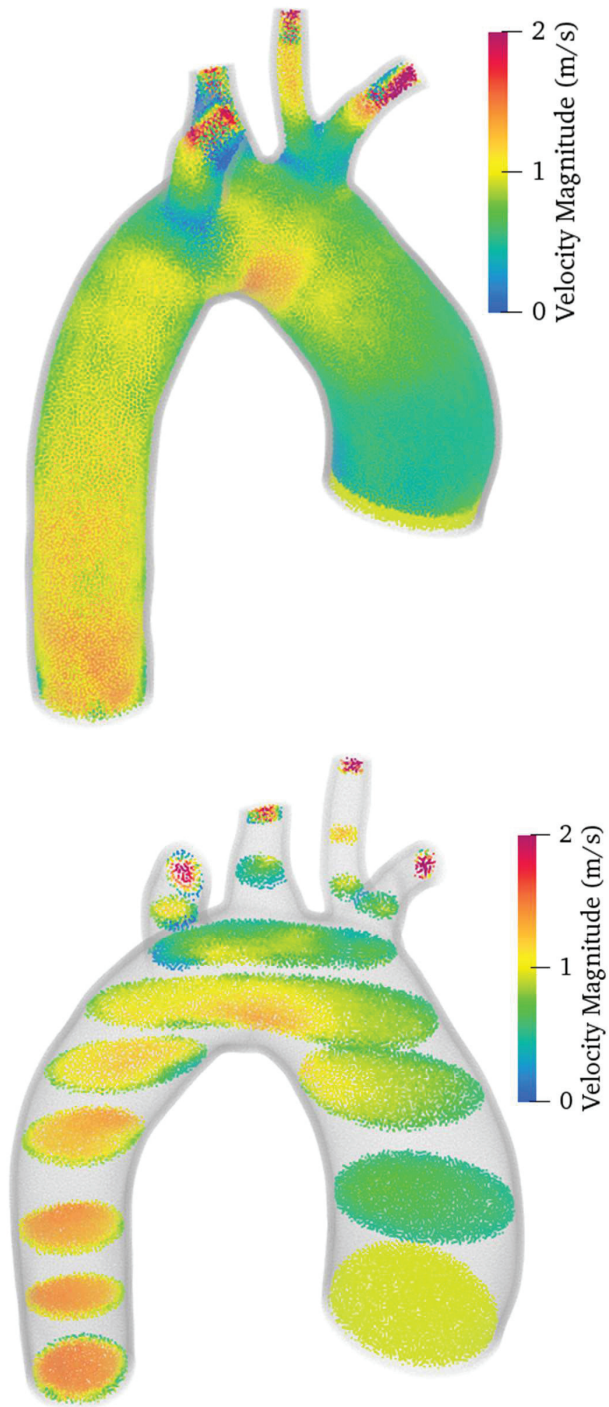


Figure 15: Velocity contour and slices of aorta flow during the peak systole. Time instant $t = 4.9s$.

References

- [1] M. T. de Almeida Jansen Catanho, M. Sinha, V. Vijayan, Model of aortic blood flow using the windkessel effect, 2012.
- [2] C. Antoci, M. Gallati, S. Sibilla, Numerical simulation of fluid–structure interaction by sph, *Computers & structures* 85 (2007) 879–890.
- [3] L. Han, X. Hu, Sph modeling of fluid-structure interaction, *Journal of Hydrodynamics* 30 (2018) 62–69.
- [4] C. Zhang, M. Rezavand, Y. Zhu, Y. Yu, D. Wu, W. Zhang, J. Wang, X. Hu, SPHinXsys: An open source multi-physics and multi-resolution library based on smoothed particle hydrodynamics, *Computer Physics Communications* 267 (2021) 108066.
- [5] D. W. Holmes, P. Pivonka, Novel pressure inlet and outlet boundary conditions for smoothed particle hydrodynamics, applied to real problems in porous media flow, *Journal of Computational Physics* 429 (2021) 110029.
- [6] M. Hirschler, P. Kunz, M. Huber, F. Hahn, U. Nicken, Open boundary conditions for isph and their application to micro-flow, *Journal of Computational Physics* 307 (2016) 614–633.
- [7] P. Kunz, M. Hirschler, M. Huber, U. Nicken, Inflow/outflow with dirichlet boundary conditions for pressure in isph, *Journal of Computational Physics* 326 (2016) 171–187.

- [8] A. Monteleone, M. Monteforte, E. Napoli, Inflow/outflow pressure boundary conditions for smoothed particle hydrodynamics simulations of incompressible flows, *Computers and Fluids* 159 (2017) 9–22.
- [9] S. Braun, L. Wieth, R. Koch, H. Bauer, A framework for permeable boundary conditions in SPH: Inlet, Outlet, Periodicity, 2015.
- [10] in: *Molecular Dynamics Simulation of Nanocomposites Using BIOVIA Materials Studio, Lammmps and Gromacs*, Micro and Nano Technologies, Elsevier, 2019.
- [11] P. Negi, P. Ramachandran, How to train your solver: Verification of boundary conditions for smoothed particle hydrodynamics, *Physics of Fluids* 34 (2022).
- [12] L. Martin, M. Basa, N. Quinlan, Permeable and non-reflecting boundary conditions in SPH, *International Journal for Numerical Methods in Fluids* 61 (2009) 709–724.
- [13] I. Federico, S. Marrone, A. Colagrossi, F. Aristodemo, M. Antuono, Simulating 2d open-channel flows through an sph model, *European Journal of Mechanics - B/Fluids* 34 (2012) 35–46.
- [14] R. Vacondio, B. Rogers, P. Stansby, P. Mignosa, SPH modeling of shallow flow with open boundaries for practical flood simulation, *Journal of Hydraulic Engineering* 138 (2012) 530–541.
- [15] C. Alvarado-Rodriguez, J. Klapp, L. Sigalotti, J. Dominguez, E. Sanchez, Nonreflecting outlet boundary conditions for incompressible flows using SPH, *Computers and Fluids* 159 (2017) 177–188.

- [16] M. Ferrand, A. Joly, C. Kassiotis, D. Violeau, A. Leroy, F. Morel, B. Rogers, Unsteady open boundaries for SPH using semi-analytical conditions and riemann solver in 2D, *Computer Physics Communications* 210 (2017) 29–44.
- [17] A. Tafuni, J. Domínguez, R. Vacondio, A. Crespo, A versatile algorithm for the treatment of open boundary conditions in smoothed particle hydrodynamics GPU models, *Computer Methods in Applied Mechanics and Engineering* 342 (2018) 604–624.
- [18] P. Negi, P. Ramachandran, A. Haftu, An improved non-reflecting outlet boundary condition for weakly-compressible SPH, *Computer Methods in Applied Mechanics and Engineering* 367 (2020) 113119.
- [19] S. Zhang, W. Zhang, C. Zhang, X. Hu, A lagrangian free-stream boundary condition for weakly compressible smoothed particle hydrodynamics, *Journal of Computational Physics* 490 (2023) 112303.
- [20] J. Monaghan, Simulating free surface flows with SPH, *Journal of Computational Physics* 110 (1994) 399–406.
- [21] J. P. Morris, P. J. Fox, Y. Zhu, Modeling Low Reynolds Number Incompressible Flows Using SPH, *Journal of Computational Physics* 136 (1997) 214–226.
- [22] X. Hu, N. Adams, A multi phase SPH method for macroscopic and mesoscopic flows, *Journal of Computational Physics* 213 (2006) 844–861.

- [23] C. Zhang, X. Hu, N. Adams, A generalized transport-velocity formulation for smoothed particle hydrodynamics, *Journal of Computational Physics* 337 (2017) 216–232.
- [24] C. Zhang, M. Rezavand, X. Hu, Dual-criteria time stepping for weakly compressible smoothed particle hydrodynamics, *Journal of Computational Physics* 404 (2020) 109135.
- [25] C. Zhang, Y. Wei, F. Dias, X. Hu, An efficient fully lagrangian solver for modeling wave interaction with oscillating wave surge converter, *Ocean Engineering* 236 (2021) 109540.
- [26] C. Zhang, X. Hu, N. Adams, A weakly compressible SPH method based on a low-dissipation Riemann solver, *Journal of Computational Physics* 335 (2017).
- [27] S. Lind, R. Xu, P. Stansby, B. Rogers, Incompressible smoothed particle hydrodynamics for free-surface flows: A generalised diffusion-based algorithm for stability and validations for impulsive flows and propagating waves., *Journal of Computational Physics* 231 (2012) 1499–1523.
- [28] G. Oger, S. Marrone, D. Le Touzé, M. de Leffe, Sph accuracy improvement through the combination of a quasi-lagrangian shifting transport velocity and consistent ale formalisms, *Journal of Computational Physics* 313 (2016) 76–98.
- [29] S. Litvinov, X. Hu, N. A. Adams, Towards consistence and convergence of conservative sph approximations, *Journal of Computational Physics* 301 (2015) 394–401.

- [30] P. Negi, P. Ramachandran, Techniques for second-order convergent weakly compressible smoothed particle hydrodynamics schemes without boundaries, *Physics of Fluids* 34 (2022) 087125.
- [31] A. Skillen, S. Lind, P. K. Stansby, B. D. Rogers, Incompressible smoothed particle hydrodynamics (sph) with reduced temporal noise and generalised fickian smoothing applied to body–water slam and efficient wave–body interaction, *Computer Methods in Applied Mechanics and Engineering* 265 (2013) 163–173.
- [32] A. Khayyer, H. Gotoh, Y. Shimizu, Comparative study on accuracy and conservation properties of two particle regularization schemes and proposal of an optimized particle shifting scheme in isph context, *Journal of Computational Physics* 332 (2017) 236–256.
- [33] P. Sun, A. Colagrossi, S. Marrone, A. Zhang, The delta plus-sph model: Simple procedures for a further improvement of the sph scheme, *Computer Methods in Applied Mechanics and Engineering* 315 (2017) 25–49.
- [34] S. Adami, X. Hu, N. Adams, A transport-velocity formulation for smoothed particle hydrodynamics, *Journal of Computational Physics* 241 (2013) 292–307.
- [35] G. Dilts, Moving-least-squares-particle hydrodynamics—I. Consistency and stability, *International Journal for Numerical Methods in Engineering* 44 (1999) 1115–1155.
- [36] A. Haque, G. Dilts, Three-dimensional boundary detection for particle methods, *Journal of Computational Physics* 226 (2007) 1710–1730.

- [37] E. Lee, C. Moulinec, R. Xu, D. Violeau, D. Laurence, P. Stansby, Comparisons of weakly compressible and truly incompressible algorithms for the SPH mesh free particle method, *Journal of Computational Physics* 227 (2008) 8417–8436.
- [38] J. J. Monaghan, Smoothed particle hydrodynamics, *Annual Review of Astronomy and Astrophysics* 30 (1992) 543–574.
- [39] H. Wendland, Piecewise polynomial, positive definite and compactly supported radial functions of minimal degree, *Advances in Computational Mathematics* 4 (1995) 389–396.
- [40] H. Takeda, S. M. Miyama, M. Sekiya, Numerical Simulation of Viscous Flow by Smoothed Particle Hydrodynamics, *Progress of Theoretical Physics* 92 (1994) 939–960.
- [41] L. D. G. Sigalotti, J. Klapp, E. Sira, Y. Meleán, A. Hasmy, SPH simulations of time-dependent Poiseuille flow at low Reynolds numbers, *Journal of Computational Physics* 191 (2003) 622–638.
- [42] D. Holmes, J. Williams, P. Tilke, Smooth particle hydrodynamics simulations of low reynolds number flows through porous media, *International Journal for Numerical and Analytical Methods in Geomechanics* 35 (2011) 419 – 437.
- [43] S. Adami, X. Hu, N. Adams, A generalized wall boundary condition for smoothed particle hydrodynamics, *Journal of Computational Physics* 231 (2012) 7057–7075.

- [44] J. R. Womersley, Method for the calculation of velocity, rate of flow and viscous drag in arteries when the pressure gradient is known, *The Journal of Physiology* 127 (1955) 553–563.
- [45] K. Laganà, R. Balossino, F. Migliavacca, G. Pennati, E. L. Bove, M. R. de Leval, G. Dubini, Multiscale modeling of the cardiovascular system: application to the study of pulmonary and coronary perfusions in the univentricular circulation, *Journal of Biomechanics* 38 (2005) 1129–1141.
- [46] D. Gallo, G. De Santis, F. Negri, D. Tresoldi, R. Ponzini, D. Massai, M. Deriu, P. Segers, B. Verheghe, G. Rizzo, U. Morbiducci, On the use of in vivo measured flow rates as boundary conditions for image-based hemodynamic models of the human aorta: Implications for indicators of abnormal flow, *Annals of biomedical engineering* 40 (2012) 729–41.
- [47] I. Taib, M. S. A. Paisal, A. E. Ismail, A. M. Tajul Arifin, N. Darlis, An analysis of blood pressure waveform using windkessel model for normotensive and hypertensive conditions in carotid artery, *Journal of Advanced Research in Fluid Mechanics and Thermal Sciences* 57 (2019) 69–85.
- [48] On coupling a lumped-parameter heart model with a three-dimensional finite element model of the aorta, *ASME Summer Bioengineering Conference*.
- [49] M. Sudharsan, E. Cherry Kemmerling, The effect of inlet and outlet boundary conditions in image-based cfd modeling of aortic flow, *BioMedical Engineering OnLine* 17 (2018).